



Cite this: *Nanoscale Horiz.*, 2026, 11, 264

Received 23rd July 2025,  
Accepted 13th October 2025

DOI: 10.1039/d5nh00527b

rsc.li/nanoscale-horizons

## Synthesis of 2D-NiPtTe<sub>2</sub> by topotactical surface reaction of PtTe<sub>2</sub> with Ni

Nirosha Ravinath Rajapakse,<sup>a</sup> Mahdi Ghorbani-Asl,<sup>b</sup> Kinga Lasek,<sup>a</sup> Arkady V. Krasheninnikov<sup>b</sup> and Matthias Batzill<sup>b</sup>      

**Topotaxy of 2D materials by reacting a van der Waals-material with a transition metal is a potential approach for accessing compositional 2D variants. Here, the synthesis of a 2D-NiPtTe<sub>2</sub> alloy is demonstrated by incorporating Ni into PtTe<sub>2</sub>. The Pt-telluride system exhibits two 2D phases, a di-telluride (PtTe<sub>2</sub>) and mono-telluride (Pt<sub>2</sub>Te<sub>2</sub>). By reacting PtTe<sub>2</sub> with Ni the system transforms into a NiPtTe<sub>2</sub>, *i.e.* the mono-telluride phase with two transition metals per unit cell in an ordered alloy structure. The samples are grown by molecular beam epitaxy and characterized by low energy electron diffraction, X-ray photoemission spectroscopy, and scanning tunneling microscopy. Studies are performed on both multilayer PtTe<sub>2</sub> films as well as monolayer samples. On multilayers the transformation is more complex and different phases can coexist. In monolayers a phase separation into pure PtTe<sub>2</sub> and the Ni-modified NiPtTe<sub>2</sub> phase is observed, indicating that both are low energy configurations. The formation energy of various structures with different Ni-composition is also evaluated by density functional theory calculations confirming that the mixed NiPtTe<sub>2</sub> phase is favored over other configurations, particularly the intercalation of Ni in between PtTe<sub>2</sub> layers is shown to be less favorable.**

2D materials have potential for the design of new quantum systems due to their ability to combine dissimilar materials without formation of covalent bonding at the interface. Naturally occurring or easily synthesized bulk crystals of layered materials form the basis of such single or few layer 2D materials, that can be either exfoliated from bulk crystals or be grown as monolayers by various chemical or physical thin film growth methods. Even though many natural layered materials exist, a need for materials with desirable properties led researchers to look beyond purely 2D systems for the fabrication of van der Waals (vdW) heterostructures. Recently, it has been shown that certain non-layered materials, *i.e.* materials that have a 3D covalent crystal structure in the bulk can be stabilized as single

### New concepts

Production of most 2D materials is based on the exfoliation of their bulk van der Waals counterparts or the growth of bulk-analog materials as monolayers. However, there is a demand for new 2D compounds with specific functionalities. In this work we demonstrate that well-known 2D materials may be transformed into a new (metastable) phase by a topotactic reaction. Specifically, we demonstrate the synthesis of a novel 2D-NiPtTe<sub>2</sub> by reaction of MBE-grown PtTe<sub>2</sub> monolayer with elemental Ni. The high spin orbit interaction in PtTe<sub>2</sub> makes the NiPtTe<sub>2</sub>/PtTe<sub>2</sub> system of interest in spintronics applications and the introduction of elements with magnetic moments is an important advancement in combining functionalities in 2D materials. The demonstrated creation of new 2D materials by topotaxy is an approach that may be extended to other 2D compounds.

layers.<sup>1–3</sup> Strong crystallographic anisotropies and easy cleavage planes allow these materials to be exfoliated or grown as a few atomic-layer thick films with vdW-like surface terminations. An example of such materials is self-intercalated transition metal dichalcogenides (TMDs). In these compositional variations of TMDs additional transition metal (TM) atoms are inserted in between the TMD layers as ‘self-intercalants’.<sup>4–9</sup> In the bulk, such materials have the NiAs-structure with periodic TM vacancies and only if the interlayer gap of the TMD is fully occupied by excess TM the NiAs-structure is obtained. Such compounds are examples of non-layered materials that can be cleaved or grown as few-layer quasi 2D-materials.

Another approach to the exfoliation of bulk materials to extend the family of layered materials is to modify well-known vdW materials by inserting different elements by a topotaxial reaction. In TMDs, such a reaction can result in self-intercalation compounds as described above, if reacted with the same TM. In addition, new meta-stable compounds, which do not exist in bulk-form, can be created by reacting bi- or multi-layers of TMDs with different TMs. This has been, for example, shown by reacting VSe<sub>2</sub> with Mn or Cr, to synthesize VSe<sub>2</sub>-bilayer intercalated with an ordered array of Mn or Cr atoms, forming a novel pseudo 2D material.<sup>10</sup> In other topotaxial reactions the reactant is directly incorporated into a 2D

<sup>a</sup> Department of Physics, University of South Florida, Tampa, FL 33620, USA.

E-mail: [mbatzill@usf.edu](mailto:mbatzill@usf.edu)

<sup>b</sup> Helmholtz-Zentrum Dresden-Rossendorf, Institute of Ion Beam Physics and Materials Research, 01328 Dresden, Germany



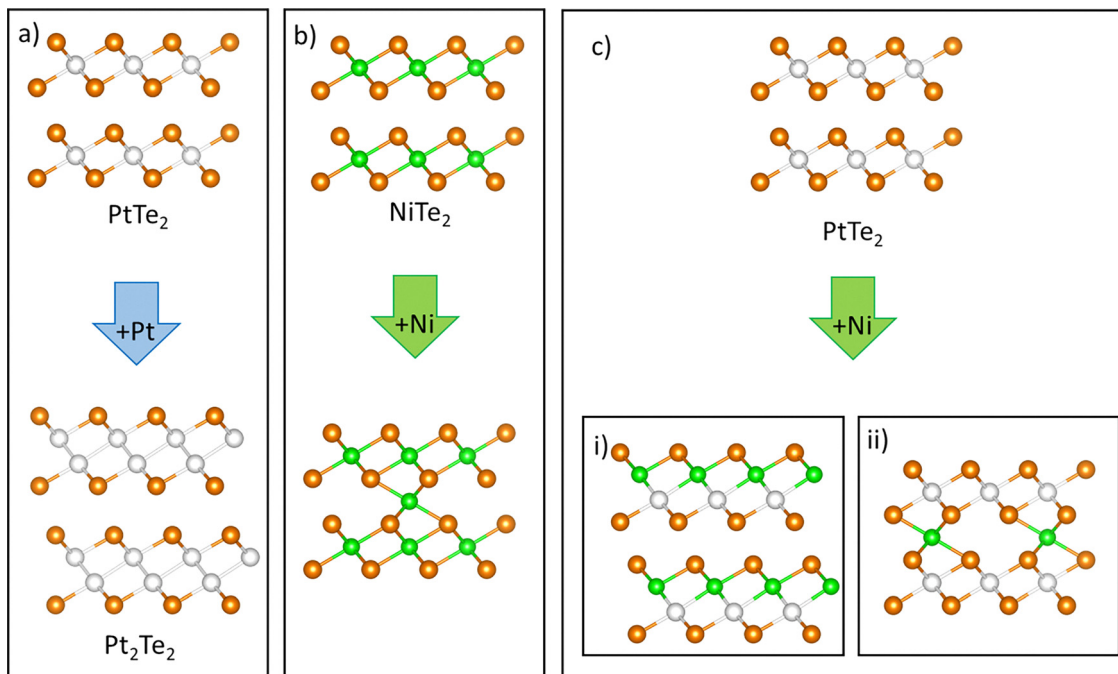


Fig. 1 Schematic of compositional variations of group 10 TMDs. (a) The  $\text{PtTe}_2$  reaction with excess Pt results in a  $\text{Pt}_2\text{Te}_2$  structure. (b) For  $\text{NiTe}_2$ , the reaction with excess Ni results in a modified NiAs structure, which may be viewed as a self-intercalation compound. Possible transformation in a mixed system (reaction of Ni with  $\text{PtTe}_2$ ) is illustrated in (c). A mixed  $\text{NiPtTe}_2$  (c)-(i), or intercalation of Ni in between  $\text{PtTe}_2$  layers (c)-(ii) are considered. White balls represent Pt atoms, green balls stand for Ni atoms, and orange balls represent Te atoms.

sheet, this has been for example shown in the homotaxy-reaction of Pt with  $\text{PtTe}_2$ , causing the formation of  $2\text{D-Pt}_2\text{Te}_2$ .<sup>11</sup>

In this work, we focus on the modification of  $\text{PtTe}_2$  with a heteroatom, namely Ni. The noble metal dichalcogenides are electronically very different from the group-IV and -V TM-chalcogenides, whose self-intercalation compounds are well documented.<sup>6,9,10</sup>  $\text{PtTe}_2$  has attracted considerable interest because of its topological and spin locking properties.<sup>12–14</sup> Also, Pt-dichalcogenides exhibit strong layer dependent properties with a transition from a semiconducting monolayer with a significant band gap (1.8 eV for  $\text{PtTe}_2$ ) to semi-metallic behavior for bi- and multilayers.<sup>15</sup> The Pt-telluride phase diagram exhibits several layered structures,<sup>16</sup> with the main phases being  $\text{PtTe}_2$  and  $\text{Pt}_2\text{Te}_2$ , whose structures are illustrated in Fig. 1(a). The direct transformation of  $\text{PtTe}_2$  to  $\text{Pt}_2\text{Te}_2$  by reaction with excess Pt has been shown in previous work.<sup>16,17</sup> Thus, in the Pt-telluride system self-intercalation is not observed. In contrast to Pt-telluride, Ni-telluride, another group-10 TMD, accommodates excess Ni by formation of self-intercalation compounds,<sup>18</sup> *i.e.* the formation of modified NiAs-like structure, see Fig. 1(b). Computed formation energies for Ni–Te system, however, suggest that the  $\text{Pt}_2\text{Te}_2$ -like structure and the NiAs structure are very close for the  $\text{Ni}_2\text{Te}_2$  stoichiometry.<sup>19</sup> Consequently, it is difficult to predict if the reaction of  $\text{PtTe}_2$  with Ni would result in Ni intercalation, *i.e.* the NiAs-structure, or in the alloying of Ni with  $\text{PtTe}_2$  to form a  $\text{NiPtTe}_2$  layer with the  $\text{Pt}_2\text{Te}_2$ -like structure, as illustrated in Fig. 1(c). In contrast to Ni, most other transition metal ditellurides prefer intercalation, so it is unlikely that the reaction of  $\text{PtTe}_2$  with transition metals other than Ni would give rise to the formation of

the  $\text{Pt}_2\text{Te}_2$ -like structure. This further motivates the choice of Ni as the reactant in this study.

Here, we investigate the Pt/Ni telluride mixed system, specifically the reaction of vapor deposited Ni with  $\text{PtTe}_2$ , with the goal of forming a novel, possibly metastable 2D material. We find that Ni reaction leads to formation of a 2D vdW material with a periodic  $\sqrt{3} \times \sqrt{3}$   $\text{R}30^\circ$  superstructure with respect to the  $1 \times 1$   $\text{PtTe}_2$  surface. Such superstructures may indicate an ordered alloy or periodic intercalation. The formation of such an ordered Ni/ $\text{PtTe}_2$  structure can be extended down to the monolayer of  $\text{PtTe}_2$ , which does not support an intercalation mechanism. X-ray photoemission spectroscopy (XPS) and density functional theory (DFT) calculations further support the formation of a novel 2D  $\text{NiPtTe}_2$  phase with a  $\text{Pt}_2\text{Te}_2$ -like structure.

## Results and discussions

$\text{PtTe}_2$  films are synthesized by molecular beam epitaxy (MBE) on vdW substrates, either graphite (HOPG) or  $\text{MoS}_2$  crystals, as reported previously.<sup>16,17</sup> Two film thicknesses are considered: (i) predominantly monolayer samples that exhibit extended  $\text{PtTe}_2$  islands with some bare substrate in between and a few bilayer regions, or (ii) 4–5 layers thick  $\text{PtTe}_2$  samples. Both kinds of samples are modified by depositing elemental Ni from an e-beam evaporator onto the surface with the sample temperature held at  $\sim 200$  °C. Surface modifications due to the reaction with Ni are observed by scanning tunneling



microscopy (STM), XPS, and low-energy electron diffraction (LEED). LEED was only possible for films grown on single crystalline  $\text{MoS}_2$  substrates, but not on HOPG because of the mosaic structure of HOPG. In the following we present the experimental results for multilayer and monolayer samples, then the phase stability and adsorption structures of some of the proposed phases are assessed by DFT calculations.

### Multilayer samples

Multilayers ( $\sim 4$  layers of  $\text{PtTe}_2$ ) have been investigated after sequential deposition of increasing amounts of Ni. The XPS spectra of pristine  $\text{PtTe}_2$  films and after 3 sequential Ni depositions are shown in Fig. 2. As we have reported previously, the Pt 4f core levels have specific binding energies for  $\text{PtTe}_2$  and  $\text{Pt}_2\text{Te}_2$  (see Fig. S1).<sup>16</sup> It is reasonable to assume that the formation of a  $\text{NiPtTe}_2$  alloy with the  $\text{Pt}_2\text{Te}_2$ -like structure would result in a similar Pt 4f binding energy. In contrast, Ni-

intercalation does not change the Pt–Te coordination and thus the Pt-4f binding energy will be less affected in an intercalation compound. Thus, XPS enables us to clarify if  $\text{NiPtTe}_2$  formation occurs after reaction with Ni. Moreover, from Pt-4f to Ni-2p peak intensity ratios the Ni:Pt atomic ratios of the sample can be estimated (see Experimental section). It should be noted that the Ni-2p<sub>1/2</sub> peak overlaps with the Te-3p<sub>1/2</sub> peak (see Fig. 2), hence only the Ni-2p<sub>3/2</sub> component has been used for determining the atomic ratios. After Ni-deposition the three samples used for obtaining the data presented in Fig. 2 have a Ni:Pt atomic ratio of 0.04, 0.11, and 0.21, as shown in Table 1. Detailed examination of the Pt-4f peak indicates that with increasing Ni concentration the peak broadens, and a second component needs to be fitted. The two components correspond well to the previously reported  $\text{PtTe}_2$  and  $\text{Pt}_2\text{Te}_2$  phases<sup>16</sup> and are thus the two Pt-4f components are labeled as Pt ( $\text{PtTe}_2$ ) and Pt ( $\text{Pt}_2\text{Te}_2$ ), in the following. While the  $\text{Pt}_2\text{Te}_2$ -like component

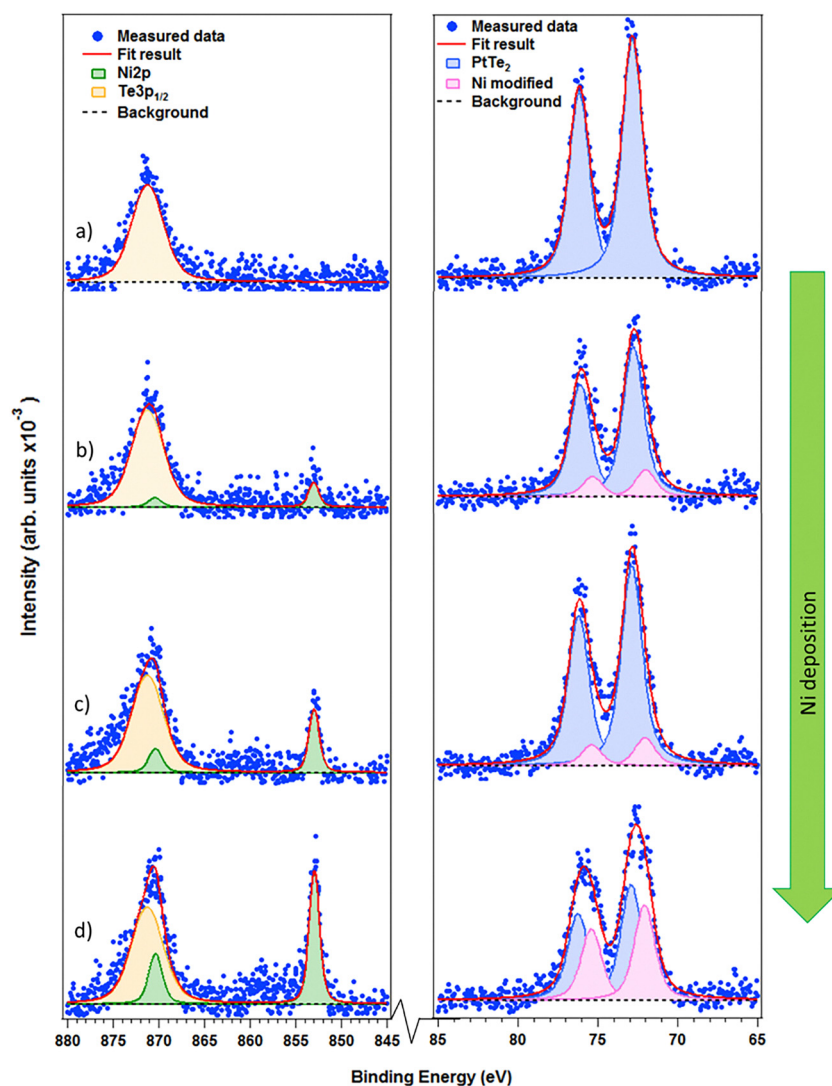


Fig. 2 XPS analysis of Pt-4f and Ni-2p region on multilayer  $\text{PtTe}_2$  sample. (a) pristine  $\text{PtTe}_2$  film and (b)–(d) for sequential Ni deposition. The Pt-4f peak is de-convoluted into two components corresponding to Pt in  $\text{PtTe}_2$  (blue) and  $\text{Pt}_2\text{Te}_2$  (pink). The Ni-2p (green) peak partially overlaps with the Te 3p<sub>1/2</sub> (yellow) peak.



**Table 1** Atomic ratios determined from XPS intensities measured on multilayer PtTe<sub>2</sub> samples. Column one indicates the Ni : Pt atomic ratios, columns 2 and 3 show the intensity of the two Pt-4f components associated with Pt in PtTe<sub>2</sub> and Pt<sub>2</sub>Te<sub>2</sub>-like environments and their ratios are shown in column 4. Columns 5 and 6 show the ratio of Ni with respect to these two Pt components

	Ni:Pt	Pt (PtTe <sub>2</sub> )	Pt (Pt <sub>2</sub> Te <sub>2</sub> )	Pt <sub>2</sub> Te <sub>2</sub> :PtTe <sub>2</sub>	Ni:Pt(PtTe <sub>2</sub> )	Ni:Pt(Pt <sub>2</sub> Te <sub>2</sub> )
Pristine	0.00	0.27	0.00	0.00	0.00	—
1st Ni exposure	0.04	0.23	0.03	0.11	0.04	0.34
2nd Ni exposure	0.11	0.17	0.04	0.26	0.14	0.53
3rd Ni exposure	0.21	0.14	0.10	0.71	0.36	0.51

increases, it always remains a minority component for the amount of Ni deposited; the Pt-ratio in the two phases is also shown in Table 1. We interpret the appearance of a Pt<sub>2</sub>Te<sub>2</sub>-like XPS peak in terms of the formation of PtTe<sub>2</sub> or a NiPtTe<sub>2</sub>-alloy. In such an alloy the Ni:Pt atomic ratio should be 1:1. The atomic ratio of the low energy component of the Pt-4f peak, *i.e.* the component associated with Pt<sub>2</sub>Te<sub>2</sub>-like phase, and the Ni peak are shown in Table 1. For different Ni-deposition, the ratios are in a range between 0.3 and 0.5, which is lower than expected for a NiPtTe<sub>2</sub> alloy, indicating that only part of the Pt<sub>2</sub>Te<sub>2</sub>-like component can be attributed to NiPtTe<sub>2</sub>. The obvious other source for a Pt<sub>2</sub>Te<sub>2</sub> component is the formation of Pt<sub>2</sub>Te<sub>2</sub> itself.

In LEED-patterns the reaction of PtTe<sub>2</sub> with Ni causes  $\sqrt{3} \times \sqrt{3}$  R30° superstructure spots as shown in Fig. 3(a and b). Such superstructure spots indicate the formation of a new phase. In large-scale STM images (Fig. 3(c and d)) it is apparent that the surface exhibits atomically flat terraces. Zooming in, however, shows that the surface is inhomogeneous, and different phases can be observed that differ in their periodicity (superstructure)

or their defect structures. Fig. 3(e) shows an STM image with different domains present. Two domains on the surface have the same  $1 \times 1$  periodicity and a third domain has a  $\sqrt{3} \times \sqrt{3}$  R30° periodicity relative to the others. The two domains with  $1 \times 1$  periodicity mainly differ in defect concentration, which is like what has been previously reported to be the case between PtTe<sub>2</sub> and Pt<sub>2</sub>Te<sub>2</sub> phases.<sup>16</sup> Thus, the STM observation suggests a complex coexistence of at least 3 phases after reaction of PtTe<sub>2</sub> with Ni. We tentatively assign these 3 phases to NiTe<sub>2</sub> (or PtTe<sub>2</sub>), Pt<sub>2</sub>Te<sub>2</sub>, and a new phase with a  $\sqrt{3} \times \sqrt{3}$  R30° superstructure. The first two phases may form according to the reaction of Ni + 2PtTe<sub>2</sub>  $\Rightarrow$  NiTe<sub>2</sub> + Pt<sub>2</sub>Te<sub>2</sub>. Such a reaction would imply a Ni:Pt(Pt<sub>2</sub>Te<sub>2</sub>) atomic ratio of  $\frac{1}{2}$ , close to the value derived from XPS. The periodic superstructure could be a periodic NiPtTe<sub>2</sub> alloy or a periodic Ni-intercalation compound. Such a compound implies a Ni/Pt (Pt<sub>2</sub>Te<sub>2</sub>) ratio of 1, which is clearly larger than measured in XPS. Importantly, there is no indication of Ni intercalation from XPS. To simplify reactions and possible reaction products, we studied reaction of Ni with monolayer PtTe<sub>2</sub>.

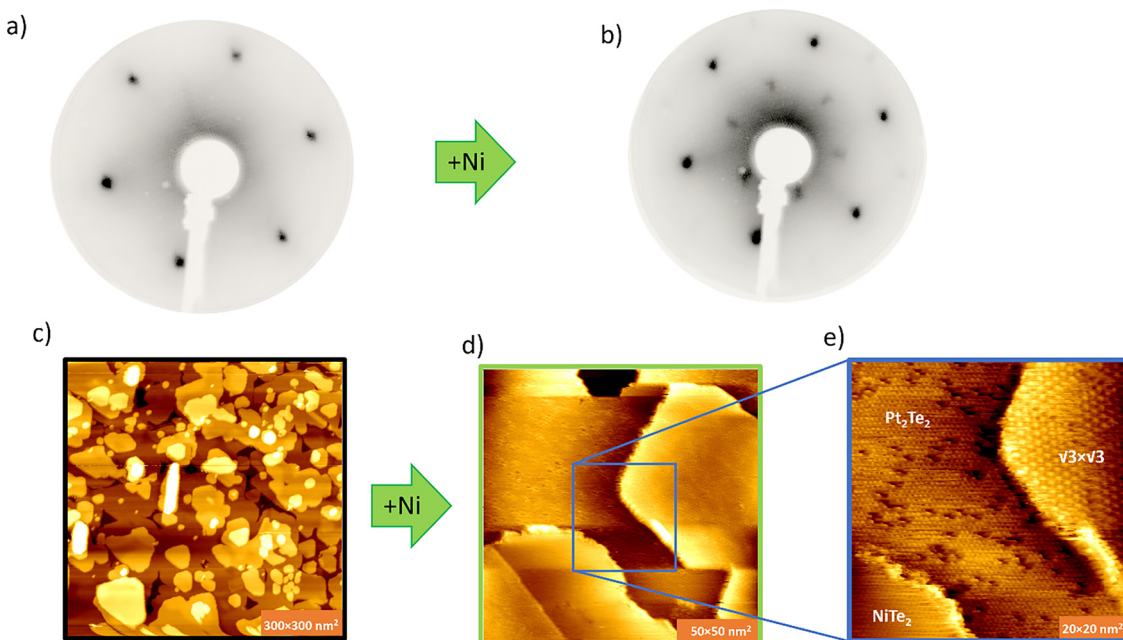


**Fig. 3** LEED and STM characterization of multilayer PtTe<sub>2</sub> modified by reaction of 3 monolayers of Ni. LEED patterns for PtTe<sub>2</sub> film before (a) and after reaction with Ni (b) indicate a (partial) film transformation to a  $\sqrt{3} \times \sqrt{3}$  R30° superstructure. STM of Ni film before (c) and after reaction with Ni (d) show that the sample remains flat but the surface exhibits different domains (e). Terraces with a  $\sqrt{3} \times \sqrt{3}$  R30° periodicities are observed, in addition to two kinds of terraces with  $1 \times 1$  structure. Structures with a high density of point defects have been previously identified with a Pt<sub>2</sub>Te<sub>2</sub> phase, while low defect densities may be either PtTe<sub>2</sub> or NiTe<sub>2</sub>.



### Ni-modification of monolayer PtTe<sub>2</sub> samples

The reaction of multilayer samples with Ni causes formation of various phases. One of these give a periodic  $\sqrt{3} \times \sqrt{3}$  R30° superstructure. Periodic intercalation may give such superstructures in multilayers, but for monolayers intercalation is not possible. Thus, here we examine the reaction of Ni with monolayer PtTe<sub>2</sub> in an effort to experimentally distinguish between intercalation and alloying.

Fig. 4(a) shows a representative STM image of a close to monolayer MBE-grown PtTe<sub>2</sub> sample with extended monolayer regions with only a few 'holes' in the monolayer and a few bilayer islands. After Ni deposition the terrace structure is modified, as shown in Fig. 4(b). The monolayer now has two phases with a significant apparent height difference of  $\sim 0.4$  nm imaged at a bias voltage of 1.0 V. In addition, some of the bilayers also show two heights, however with only a small height difference of  $\sim 0.1$  nm. The larger apparent height difference in modified monolayers is due to the strong electrostatic differences between monolayers and multilayers PtTe<sub>2</sub>.

Monolayer PtTe<sub>2</sub> is semiconducting with a 1.8 eV band gap while bilayers are (semi)metallic.<sup>15</sup> A transformation of the monolayer by either intercalation of Ni or conversion into NiPtTe<sub>2</sub> makes it metallic and thus an apparent contrast between the semiconducting PtTe<sub>2</sub>-monolayer and metallic transformed regions is expected as has been previously reported for PtTe<sub>2</sub>/Pt<sub>2</sub>Te<sub>2</sub> monolayer junctions.<sup>11</sup> In contrast, bilayer PtTe<sub>2</sub> is already metallic and thus the apparent height difference in STM images between different phases are expected to be less. Further Ni deposition completely disrupts the terraces and causes a restructuring and formation of elongated crystallites (see Fig. 4(c)). These are likely non-layered Ni-rich phases, and these materials are beyond the scope of this communication.

The large-scale images show that the monolayer region separated into two phases with strong apparent layer height differences. This indicates that Ni reaction causes a well-defined compositional phase that segregates from pristine PtTe<sub>2</sub>, suggesting that the new compositional phase is a

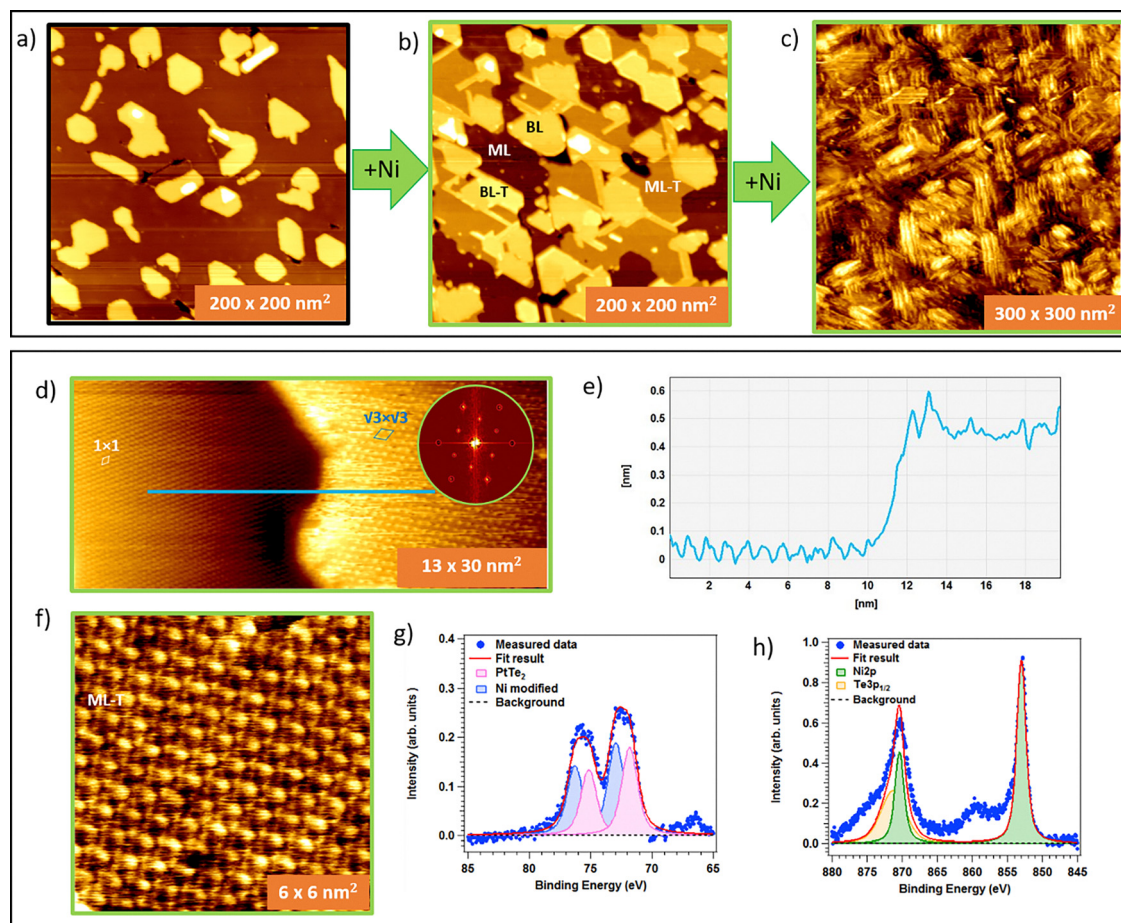


**Fig. 4** Reaction of (predominantly) monolayer PtTe<sub>2</sub> with Ni. (a) STM image of monolayer samples with some bilayer islands of pristine PtTe<sub>2</sub>. (b) After reaction with 0.5 monolayer of Ni, the monolayer region exhibits modified region with a large apparent contrast and un-modified regions (ML-monolayer, BL-bilayer, MLT/BLT – mono/bilayer transformed). Further Ni deposition (c) causes disruption of the layer structure. High resolution STM image of the monolayer region after Ni modification is shown in (d) with corresponding FFT in the inset and panel (e) presents the apparent height profile along the line indicated in (d). Pristine PtTe<sub>2</sub> regions with a 1 × 1 periodicity and the Ni-modified region with a  $(\sqrt{3} \times \sqrt{3})$ R30 superstructure are observed in (d) and (e). High resolution image of the  $(\sqrt{3} \times \sqrt{3})$ R30 superstructure is shown in (f). XPS of Pt-4f (g) and Ni-2p (h) for the partially Ni-modified sample.



compositional line phase. High-resolution STM of this Ni modified phase shows that it exhibits a  $\sqrt{3} \times \sqrt{3}$  R30° periodicity, which is also visible in LEED. The sharp phase-boundary between the  $1 \times 1$ -PtTe<sub>2</sub> and the  $\sqrt{3} \times \sqrt{3}$  R30° Ni:PtTe<sub>2</sub> phase is clearly observed in Fig. 4(d). XPS of partially Ni modified PtTe<sub>2</sub> again shows two Pt-components associated with PtTe<sub>2</sub> and Pt<sub>2</sub>Te<sub>2</sub>-like components. The latter only appears after Ni adsorption and reaction. The Ni/Pt (Pt<sub>2</sub>Te<sub>2</sub>) atomic ratio is determined from XPS to 1.05. Thus, in contrast to the reaction with multilayer PtTe<sub>2</sub>, the Ni/Pt (Pt<sub>2</sub>Te<sub>2</sub>) ratio is consistent with the formation of NiPtTe<sub>2</sub> alloy. The formation of a single alloy phase in the monolayer is also consistent with STM, which only shows a single Ni-modified structure with a  $\sqrt{3} \times \sqrt{3}$  R30° periodicity. This indicates while different reaction paths are possible in the multilayer there is only one outcome for Ni reacting with PtTe<sub>2</sub>, which appears to be an ordered NiPtTe<sub>2</sub> phase. The Te-3d peak has been monitored but no significant change has been observed due to reacting PtTe<sub>2</sub> with Ni (Fig. S2). In the experimental approach of adding Ni from the gas phase, the stable phase should be the one with the lowest energy per Ni-atom. To compare the formation energies of

different structures and Ni compositions we performed DFT calculations.

### DFT calculations

We distinguish between four different basic structures of Ni incorporation into PtTe<sub>2</sub>: (i) an alloy, in which Ni replaces Pt in PtTe<sub>2</sub>, (ii) Ni-adsorption on the surface of a PtTe<sub>2</sub> layer, *i.e.* Ni is only coordinated to a single PtTe<sub>2</sub> layer; (iii) Ni intercalation between two PtTe<sub>2</sub> layers, *i.e.* Ni is coordinated to two PtTe<sub>2</sub> layers; (iv) formation of NiPtTe<sub>2</sub> alloy with a Pt<sub>2</sub>Te<sub>2</sub>-structure. In the first three configurations the amount of Ni can be varied by different occupations of lattice or adsorption sites, while in the last configuration Ni:Pt = 1:1.

To gain microscopic insights into the formation of possible different mixed Ni-Pt-Te phases we performed DFT calculations of their formation energies  $E_f$ , as described in the Methods section.  $E_f$  was computed per Ni-atom as a function of Ni concentration for structures (ii) and (iii) for bilayer PtTe<sub>2</sub> (we chose bilayer for comparison of the different structures, since the Ni intercalation structure is only possible in bilayers).

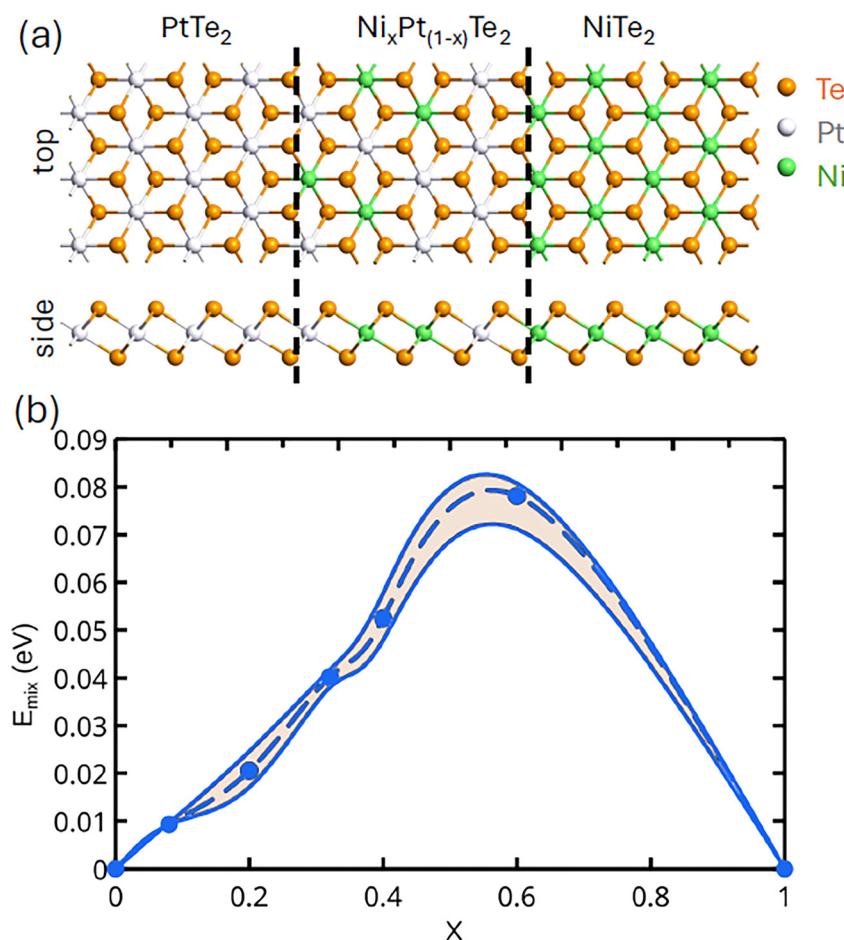


**Fig. 5** Mixing energies of Ni<sub>x</sub>Pt<sub>(1-x)</sub>Te<sub>2</sub> TMD layer, indicating energetically unfavorable alloy formation and preferred segregation into elemental-pure TMDs. (a) The atomic structures of PtTe<sub>2</sub> (left), Ni<sub>x</sub>Pt<sub>(1-x)</sub>Te<sub>2</sub> mixed alloy (middle), and NiTe<sub>2</sub> (right) in top and side views. (b) Internal mixing energies per primitive cell for Ni<sub>x</sub>Pt<sub>(1-x)</sub>Te<sub>2</sub> alloys. The width of the shaded areas indicates the standard deviation of the variation in calculated energies. White balls represent Pt atoms, green balls Ni atoms, and orange balls stand for Te atoms.



(i)  $\text{Ni}_x\text{Pt}_{1-x}\text{Te}_2$  alloy phases: to evaluate the potential incorporation of Ni atoms into the  $\text{PtTe}_2$  lattice, we investigated the formation of mixed  $\text{Ni}_x\text{Pt}_{1-x}\text{Te}_2$  alloy phases. The atomic structures of the alloys, along with those of the parent compounds, are schematically shown in Fig. 5(a).

Fig. 5(b) presents the calculated mixing energies of the alloy as a function of the relative concentration of Ni atoms, as defined in the computational methods section. The mixing energies for the  $\text{Ni}_x\text{Pt}_{1-x}\text{Te}_2$  alloys calculated at zero temperature are positive but relatively small across the entire composition range, implying that alloy formation is energetically less favorable than phase separation into pure  $\text{NiTe}_2$  and  $\text{PtTe}_2$  phases. The results suggest that the formation of such mixed phases is unlikely.

(ii) Ni-adsorption on  $\text{PtTe}_2$ : Ni deposited on  $\text{PtTe}_2$  will adsorb at the lowest energy site on the surface and this may conceivably cause ordered adsorption structures for weak repulsive interactions between Ni adsorbates. We calculated adsorption energies on three different adsorption sites, as illustrated in Fig. S3, and found that Ni-adsorption at Te-sites on the opposing side of  $\text{PtTe}_2$  layer is the lowest energy configuration. In this configuration, the adsorbed Ni-atom has the highest coordination number to Te-atoms (4) of the possible adsorption configurations, and this may explain why it is favored. Experimentally, we observe ordered structures with a  $\sqrt{3} \times \sqrt{3} \text{ R}30^\circ$  periodicity. To investigate the relationship between the energetics and the concentration of Ni atoms, we calculated the formation energy of the system as a function of the Ni : Pt atomic ratio, by increasing the number of Ni atoms (see Fig. 6). The results show a continuous decrease in the adsorption energy per Ni atom with increasing Ni coverage, from 1/3 to full (3/3) occupation of the adsorption sites. The structure with full Ni coverage (3/3) exhibits the lowest formation energy, indicating its high stability. This seems to

contradict a  $\sqrt{3} \times \sqrt{3} \text{ R}30^\circ$  superstructure, which one naively associates with a 1/3 occupation. At the same time, there is no minimum in the adsorption energy for this composition. Interestingly for a full layer (3/3) of Ni the Ni-atoms relax laterally by pushing up some surface Te-atoms and thus forming a  $\sqrt{3} \times \sqrt{3} \text{ R}30^\circ$  superstructure. Hence, even a full layer of Ni would exhibit  $\sqrt{3} \times \sqrt{3} \text{ R}30^\circ$  superstructure in STM, confirmed by simulated STM images (Fig. S4). However, discussions below show that this Ni-adsorption structure is not the lowest energy configuration and thus although it can give the right periodicity it is unlikely to be the experimentally observed configuration.

(iii) Ni: $\text{PtTe}_2$  intercalation structure: for multilayer  $\text{PtTe}_2$ , Ni may intercalate between the layers, and such intercalated Ni atoms are coordinated to 6 Te-atoms (3 to each  $\text{PtTe}_2$ -layer). To determine whether intercalation is favored over surface adsorption, we compared the energies of structures in which Ni atoms are intercalated between two  $\text{PtTe}_2$  layers, as shown in Fig. 6. The negative values of formation energy indicate that intercalation is energetically favorable, and the energy release increases with the concentration of Ni atoms. At low Ni concentrations, intercalation between the layers is preferred over surface adsorption. However, this trend reverses at higher Ni concentrations, when Ni : Pt exceeds 1 : 3, corresponding to more than one-third of a monolayer coverage of Ni. It is also evident that the stability of intercalated Ni atoms changes only marginally beyond this threshold, indicating a saturation effect at Ni coverages above one-third of a monolayer.

(iv) Different structures for full layer of Ni including  $\text{NiPtTe}_2$ : for both surface adsorption as well as intercalation the energy per Ni atom keeps decreasing with the number of Ni atoms and reaches the lowest value for all the adsorption/intercalation sites occupied, *i.e.* for a full monolayer of Ni. This implies a phase segregation into a pure  $\text{PtTe}_2$  and a Ni-modified phase,

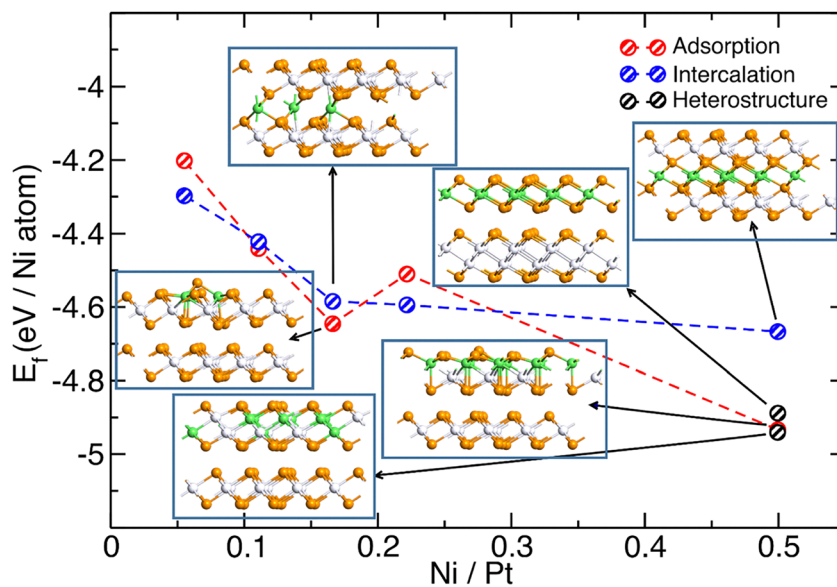
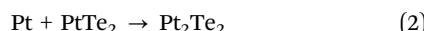
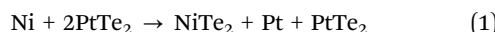


Fig. 6 Energetics for adsorption/intercalation of Ni atoms on/into  $\text{PtTe}_2$  bilayer as a function of the Ni : Pt atomic ratio. White balls represent Pt atoms, green balls Ni atoms, and orange balls Te atoms.



as observed experimentally. The Ni-modified phase should contain a full layer of Ni. In this subsection, we thus compare different  $\text{PtTe}_2$  bilayer structures modified with a full layer of Ni, *i.e.*  $\text{Ni}/\text{Pt} = 0.5$  (for the bilayer structures used in the computation). The energies of these structures are also shown in Fig. 6. Interestingly, the Ni-intercalated structure, *i.e.* a NiAs-like structure, is the least energetically favorable configuration. A full layer of Ni-adsorbed at the surface on just one  $\text{PtTe}_2$  layer is lower in energy than the intercalation structure. In this adsorption configuration the Ni-atoms are already ‘sinking’ into the  $\text{PtTe}_2$  layer and are below the surface Te-atoms and thus may be described as a vdW-alloy rather than an Ni-adsorption structure. In the following we call this structure the relaxed Ni-adsorption structure- simulated STM contrast is shown in Fig. S4. An alternative alloy structure is a replacement of Pt atoms with Ni in a  $\text{Pt}_2\text{Te}_2$  structure forming a  $\text{NiPtTe}_2$ -phase. This phase has a similar energy to the relaxed Ni-adsorption layer. Simulated STM images of a  $\sqrt{3} \times \sqrt{3}$   $30^\circ$  ordered  $\text{NiPtTe}_2$  alloy are shown in Fig. S5. Comparison of simulated STM images with the experimental results suggest that the relaxed Ni-adsorption structure (Fig. S4) is in better agreement with the experiments than the  $\text{NiPtTe}_2$ -alloy (Fig. S5). We also calculated the electronic structure of both  $\text{NiPtTe}_2$  compositional alloy structures (Fig. S6). These calculations confirm that the  $\sqrt{3} \times \sqrt{3}$   $30^\circ$  superstructures are metallic and thus explain the large electronic contrast in the STM measurements compared to semiconducting  $\text{PtTe}_2$  monolayer.

Finally, we also calculated the energy of a  $\text{NiTe}_2/\text{Pt}_2\text{Te}_2$  vdW heterostructure which could form if vapor deposited Ni extracts Te from a  $\text{PtTe}_2$  layer and the liberated Pt then transforms  $\text{PtTe}_2$  into  $\text{Pt}_2\text{Te}_2$ , *i.e.* a reaction sequence of:



reaction (2) has been previously demonstrated.<sup>11</sup>

The DFT calculations show that this heterostructure has a slightly larger energy per Ni atom compared to the  $\text{NiPtTe}_2/\text{PtTe}_2$  heterostructure (with  $\text{NiPtTe}_2$  either in a  $\text{Pt}_2\text{Te}_2$ -like or a relaxed Ni adsorption structure). However, given the only small differences in energy, both reactions may occur in multilayer samples, and this may explain the coexistence of many phases on the surface after reaction of Ni with multilayer  $\text{PtTe}_2$ . In the monolayer, however, the formation of  $\text{NiTe}_2$  is suppressed as it requires a second layer of  $\text{PtTe}_2$  to absorb the released Pt. Thus, in the monolayer we transform selectively  $\text{PtTe}_2$  into  $\text{NiPtTe}_2$ .

## Magnetic properties

X-ray magnetic circular dichroism (XMCD) measurements were conducted on Ni-modified  $\text{PtTe}_2$  samples. Unfortunately, monolayers are not sufficiently stable to allow transfer to a synchrotron facility through air, so the studies were performed on multilayers, which have been demonstrated previously to be stable in air and can be cleaned from adsorbates by vacuum annealing.<sup>17</sup> Ni was deposited on such multilayer samples at

the synchrotron end-station. Ni-XMCD (Fig. S7) indicates that at low temperatures and in a high magnetic field Ni has an average magnetic moment of  $\sim 0.4\mu_{\text{B}}$ , however, the magnetization diminishes for low magnetic fields, indicating a negligible remanence. Moreover, as demonstrated above, multilayer samples exhibit different phases, and it is not possible to identify which phase is responsible for the observed magnetic properties. Thus, further magnetic characterization is required to gain detailed insight into the magnetic properties of this novel material.

## Conclusions

Ni reaction with  $\text{PtTe}_2$ -films was investigated as a synthesis method for obtaining novel 2D materials. Vapor deposited Ni-atoms incorporate into the  $\text{PtTe}_2$  film to form ordered mixed transition metal 2D materials. Shifts in the Pt-4f core level binding energy are indicative of the transformation from a ditelluride to a mono-telluride compound, while the observation of a superstructure indicates the formation of an ordered alloy. This interpretation of an Ni-Pt alloy is supported by DFT calculations that show that the formation of a mixed mono-telluride is energetically favored over intercalation of Ni atoms in between  $\text{PtTe}_2$  bilayers.

This kind of transformation reaction of a well-established 2D material into a novel 2D material with a higher metal content (here a dichalcogenide to a monochalcogenide) by surface reaction with a transition metal has the potential for creating new functional materials. For this process to work, the reaction must result in an energy-lowering configuration, meaning a meta-stable 2D material must be accessible as the reaction product. The observed segregation into pure  $\text{PtTe}_2$  and an  $\text{NiPtTe}_2$  phase, indicates that both phases are local energy minima in a Ni-Pt-Te phase diagram, which facilitates the topotactic transformation of  $\text{PtTe}_2$  into  $\text{NiPtTe}_2$ . In the monolayer, a phase separation into the pure  $\text{PtTe}_2$  and the Ni-modified  $\text{NiPtTe}_2$  phase is observed, leaving a sharp in-plane heterojunction. This is similar to the case of modifying  $\text{PtTe}_2$  with Pt, causing the phase separation into the known 2D-phases of  $\text{PtTe}_2$  and  $\text{Pt}_2\text{Te}_2$  in the Pt-Te phase diagram.<sup>11</sup> Modifying with Ni instead of excess Pt, has the potential of inducing new functionalities, like magnetism. The  $\text{NiPtTe}_2/\text{PtTe}_2$  heterojunction may be an exciting material for spin injection into the semiconducting  $\text{PtTe}_2$  monolayer with a large spin-orbit coupling. In general, topotaxy in 2D materials, *i.e.*, the controlled transformation of one 2D material into another by reaction with a transition metal, holds promise for the synthesis of novel 2D materials and the potential of synthesis of in-plane heterojunctions.

## Methods

$\text{PtTe}_2$  sample preparation was conducted by co-deposition of Pt and Te in an ultrahigh vacuum MBE chamber (base pressure  $5 \times 10^{-9}$  mbar) on  $\text{MoS}_2$  or HOPG substrates at a growth temperature of 200 °C. Substrates were freshly cleaved in air



and subsequently degassed in vacuum at 360 °C for at least 3 hours before growth. STM characterization of MoS<sub>2</sub> substrates after outgassing did not show any sign of an increased defect/S-vacancy concentration. The growth rate for PtTe<sub>2</sub> was slow with a monolayer achieved in 60 min. The as-grown PtTe<sub>2</sub> samples were then systematically exposed to Ni keeping the sample at the growth temperature (200 °C). Ni was deposited at a rate of one ML hour<sup>-1</sup>, where a ML is defined as the amount of Ni in a single layer of NiTe<sub>2</sub>. Both Pt and Ni are evaporated from e-beam evaporators while Te is evaporated from a Knudsen cell at a temperature of 260 °C. Pt:Te flux ratio was around 1:10 during PtTe<sub>2</sub> growth. All sample characterizations were conducted by transferring the grown samples *in situ* from the growth chamber to the surface analysis chamber in which room temperature STM, LEED and XPS studies were performed. Room temperature STM was conducted using an Omicron STM-1 with electrochemically etched tungsten tips. XPS studies were conducted using Al K $\alpha$  radiation from a non-monochromatized dual anode X-ray source, and photoemitted electrons were detected with a Scienta R3000 hemispherical analyzer. The measured XPS spectra were analyzed using the KolXPD software. A Shirley background was subtracted from the raw XPS data and Voigt function was used to fit each XPS peak. The peak fitting parameters such as the amplitude (intensity), peak split distances were set depending on the spin-orbit splitting ratio and the standard splitting distances of each element. Initially, the XPS data for the as-grown PtTe<sub>2</sub> was fitted and used as a reference for fitting the PtTe<sub>2</sub> component in Ni-modified samples. For each deposition of Ni, the Pt 4f peak shows a broadening, requiring a fit with two components, reminiscent to the broadening observed in the transformation of PtTe<sub>2</sub> to Pt<sub>2</sub>Te<sub>2</sub> (see Fig. S1). The FWHM of Pt 4f (PtTe<sub>2</sub>) peaks determined from the as-grown sample was used to fit one Pt 4f (PtTe<sub>2</sub>) component after Ni deposition. The second Pt 4f component was determined for the sample with the highest Ni concentration and thus with the most intense Pt<sub>2</sub>Te<sub>2</sub>-like component in the Pt 4f peak. Such determined FWHM of the Pt<sub>2</sub>Te<sub>2</sub>-like component was then used to deconvolute all the Pt 4f peaks into their two components. The Te3d peak shape and positions were also observed (see Fig. S2) but no significant change in its peak shape or position was measured. For the Ni 2p peak the overlap of the Ni 2p<sub>1/2</sub> with Te 3p<sub>1/2</sub> only allowed us to clearly measure the intensity of the Ni 2p<sub>3/2</sub> peak. Thus, to obtain the total Ni intensity the intensity of Ni 2p<sub>3/2</sub> was multiplied by 3/2. To obtain the atomic ratios of Ni to Pt (in their two components) the XPS intensities were normalized to their atomic sensitivity factors and the analyzer transmission function. The atomic sensitivity factors were found using computed atomic sensitivity factors<sup>20</sup> for Ni 2p (0.2998) and Pt 4f (0.227). For the instrument's transmission function we used published calibrations for the Scienta R3000 analyzer used in this study<sup>21</sup> and that gives a 2-times higher transmission for photoelectrons with a kinetic energy of 633 eV (Ni 2p with Al-K $\alpha$ ) compared to kinetic energies of 1413.75 eV (Pt 4f with Al-K $\alpha$ ). This analysis indicates that the XPS intensity ratio for Ni/Pt need to be multiplied by a factor of 1/1.51 to obtain atomic ratios.

The reproducibility of the experimental studies was confirmed by repeated Ni deposition on eight different PtTe<sub>2</sub> samples (3 on MoS<sub>2</sub> and 5 on HOPG substrates) with similar results. STM data were confirmed on several distinct areas of the samples (see Fig. S8).

## Computational details

The calculations of the energies involved in the interaction of Ni with PtTe<sub>2</sub> was performed by using density-functional theory (DFT) with the PBE<sup>22</sup> exchange-correlation functional, as implemented in the VASP code<sup>23,24</sup>. As for adsorption energies, a 5 × 5 supercell has been used. A plane-wave cut-off energy of 450 eV and force tolerance of 0.01 eV Å<sup>-1</sup> was set for optimized structures. The Brillouin zones of the supercells were sampled using a 4 × 4 × 1 Monkhorst-Pack grid points. van der Waals interactions were considered using the DFT-D2 method proposed by Grimme.<sup>25</sup> In the simulations, different possibilities of Ni positions have been considered and the most stable structures have been used for intercalation energy calculations. We assessed the stability of various intercalated structures by calculating their formation energy ( $E_f$ ) per Ni atom defined as

$$E_f = E_{\text{tot}} - [E_{\text{PtTe}_2} + n_{\text{Ni}}\mu_{\text{Ni}}]/n_{\text{Ni}}$$

where  $E_{\text{tot}}$  is the total energy of the supercell containing PtTe<sub>2</sub> and Ni atoms,  $E_{\text{PtTe}_2}$  is the energy of the pristine bilayer PtTe<sub>2</sub>,  $n_{\text{Ni}}$  is the number of Ni atoms, and  $\mu_{\text{Ni}}i$  is their chemical potential, taken from isolated Ni atoms.  $E_f$  represents the energy released per atom when isolated Ni atoms are inserted into the PtTe<sub>2</sub> host structure. Simulations of constant-current scanning tunneling microscopy (STM) images were carried out using the Tersoff-Hamann approximation.

The alloy structures were modeled using 5 × 5 supercells. To gather statistical data, five different supercells with randomly distributed Ni atoms were generated for each alloy composition. The internal energy of mixing is defined as:

$$E_{\text{mix}}(x) = E_{\text{Ni}_x\text{Pt}_{1-x}\text{Te}_2} - [xE_{\text{NiTe}_2} + (1-x)E_{\text{PtTe}_2}]$$

where  $E_{\text{NiTe}_2}$  and  $E_{\text{PtTe}_2}$  are the total energies per formula unit of the binary host compounds, and  $x$  is the relative concentration of Ni atoms, defined as the ratio of the number of Ni atoms to the total number of transition metal atoms (0 <  $x$  < 1).

## Conflicts of interest

There are no conflicts to declare.

## Data availability

Data for the article is available at Harvard Dataverse repository. XPS data on multilayer PtTe<sub>2</sub> sample (corresponding to Fig. 2) is available at <https://doi.org/10.7910/DVN/A8JVZ1>. The XPS data for monolayer PtTe<sub>2</sub> sample (corresponding to Fig. 4g and h) is available at <https://doi.org/10.7910/DVN/JZ4182>. The STM image data of multilayer PtTe<sub>2</sub> (corresponding to Fig. 3c–e) is



available at <https://doi.org/10.7910/DVN/OWOV4B>. The STM image data for monolayer PtTe2 (corresponding to Fig. 4a–f) is available at <https://doi.org/10.7910/DVN/ETAKLN>. The code VASP (source files and the license) used in the first-principles calculations can be obtained from the code developers, see <https://www.vasp.at/>. The version of the code employed for this study is VASP6.4. Atomic coordinates of the structures can be obtained from the Authors upon request.

Supplementary information (SI) is available. See DOI: <https://doi.org/10.1039/d5nh00527b>.

## Acknowledgements

The USF group acknowledges support from NSF under the award DMR 2118414. In addition, AVK acknowledges funding from the German Research Foundation (DFG), Project KR 4866/6-1, and through the collaborative research center “Chemistry of Synthetic 2D Materials” SFB-1415-417590517. Generous CPU time grants from the Paderborn Center for Parallel Computing (PC2, Noctua 2 cluster, hpc-prf-def2dhet) and Gauss Centre for Supercomputing e.V. (<https://www.gauss-centre.eu>), Supercomputer HAWK at Höchstleistungsrechenzentrum Stuttgart (<https://www.hlr.de>), are greatly appreciated.

## References

- 1 N. Zhou, R. Yang and T. Zhai, *Mater. Today Nano*, 2019, **8**, 100051, DOI: [10.1016/j.mtnano.2019.100051](https://doi.org/10.1016/j.mtnano.2019.100051).
- 2 J. Y. Chung, Y. Yuan, T. P. Mishra, C. Joseph, P. Canepa, P. Ranjan, E. H. S. Sadki, S. Gradečák and S. Garaj, *Nat. Commun.*, 2024, **15**, 6122, DOI: [10.1038/s41467-024-49974-8](https://doi.org/10.1038/s41467-024-49974-8).
- 3 A. P. Balan, A. B. Puthirath, S. Roy, G. Costin, E. F. Oliveira, M. A. S. R. Saadi, V. Sreepal, R. Friedrich, P. Serles, A. Biswas, S. A. Iyengar, N. Chakingal, S. Bhattacharyya, S. K. Saju, S. C. Pardo, L. M. Sassi, T. Filleter, A. Krasheninnikov, D. S. Galvao, R. Vajtai, R. R. Nair and P. M. Ajayan, *Mater. Today*, 2022, **58**, 164–200, DOI: [10.1016/j.mattod.2022.07.007](https://doi.org/10.1016/j.mattod.2022.07.007).
- 4 Y. Ueda and T. Ohtani, in *Handbook of Solid State Chemistry*, ed R. Dronskowski, S. Kikkawa, A. Stein, Wiley-VCH, 1 edn, 2017, vol. 1, ch. 9, pp. 383–433, DOI: [10.1002/9783527691036.hsscvol1010](https://doi.org/10.1002/9783527691036.hsscvol1010).
- 5 A. Hayashi, K. Imada, K. Inoue, Y. Ueda and K. Kosuge, *Bull. Inst. Chem. Res. Kyoto Univ.*, 1986, **64**, 186–206.
- 6 K. Lasek, P. M. Coelho, K. Zberecki, Y. Xin, S. K. Kolekar, J. Li and M. Batzill, *ACS Nano*, 2020, **14**, 8473–8484, DOI: [10.1021/acsnano.0c02712](https://doi.org/10.1021/acsnano.0c02712).
- 7 M. Bonilla, S. Kolekar, J. Li, Y. Xin, P. M. Coelho, K. Lasek, K. Zberecki, D. Lizzit, E. Tosi, P. Lacovig, S. Lizzit and M. Batzill, *Adv. Mater. Interfaces*, 2020, **7**, 2000497, DOI: [10.1002/admi.202000497](https://doi.org/10.1002/admi.202000497).
- 8 C. Zhang, C. Liu, J. Zhang, Y. Yuan, Y. Wen, Y. Li, D. Zheng, Q. Zhang, Z. Hou, G. Yin, K. Liu, Y. Peng and X. X. Zhang, *Adv. Mater.*, 2023, **35**, 2205967, DOI: [10.1002/adma.202205967](https://doi.org/10.1002/adma.202205967).
- 9 X. Zhao, P. Song, C. Wang, A. C. Riis-Jensen, W. Fu, Y. Deng, D. Wan, L. Kang, S. Ning, J. Dan, T. Venkatesan, Z. Liu, W. Zhou, K. S. Thygesen, X. Luo, S. J. Pennycook and K. P. Loh, *Nature*, 2020, **581**, 171–177, DOI: [10.1038/s41586-020-2241-9](https://doi.org/10.1038/s41586-020-2241-9).
- 10 V. Pathirage, S. Khatun, S. Lisenkov, K. Lasek, J. Li, S. Kolekar, M. Valvidares, P. Gargiani, Y. Xin, I. Ponomareva and M. Batzill, *Nano Lett.*, 2023, **23**, 9579–9586, DOI: [10.1021/acs.nanolett.3c03169](https://doi.org/10.1021/acs.nanolett.3c03169).
- 11 K. Lasek, J. Li, M. Ghorbani-Asl, S. Khatun, O. Alanwoko, V. Pathirage, A. V. Krasheninnikov and M. Batzill, *Nano Lett.*, 2022, **22**, 9571–9577, DOI: [10.1021/acs.nanolett.2c03715](https://doi.org/10.1021/acs.nanolett.2c03715).
- 12 M. Yan, H. Huang, K. Zhang, E. Wang, W. Yao, K. Deng, G. Wan, H. Zhang, M. Arita, H. Yang, Z. Sun, H. Yao, Y. Wu, S. Fan, W. Duan and S. Zhou, *Nat. Commun.*, 2017, **8**, 257, DOI: [10.1038/s41467-017-00280-6](https://doi.org/10.1038/s41467-017-00280-6).
- 13 H. Xu, J. Wei, H. Zhou, J. Feng, T. Xu, H. Du, C. He, Y. Huang, J. Zhang, Y. Liu, H. C. Wu, C. Guo, X. Wang, Y. Guang, H. Wei, Y. Peng, W. Jiang, G. Yu and X. Han, *Adv. Mater.*, 2020, **32**, 2000513, DOI: [10.1002/adma.202000513](https://doi.org/10.1002/adma.202000513).
- 14 R. Feng, Y. Zhang, J. Li, Q. Li, C. Bao, H. Zhang, W. Chen, X. Tang, K. Yaegashi, K. Sugawara, T. Sato, W. Duan, P. Yu and S. Zhou, *Nat. Commun.*, 2025, **16**, 2667, DOI: [10.1038/s41467-025-57835-1](https://doi.org/10.1038/s41467-025-57835-1).
- 15 J. Li, S. Kolekar, M. Ghorbani-Asl, T. Lehnert, J. Biskupek, U. Kaiser, A. V. Krasheninnikov and M. Batzill, *ACS Nano*, 2021, **15**, 13249–13259, DOI: [10.1021/acsnano.1c02971](https://doi.org/10.1021/acsnano.1c02971).
- 16 K. Lasek, M. Ghorbani-Asl, V. Pathirage, A. V. Krasheninnikov and M. Batzill, *ACS Nano*, 2022, **16**, 9908–9919, DOI: [10.1021/acsnano.2c04303](https://doi.org/10.1021/acsnano.2c04303).
- 17 V. Pathirage, N. Ravinath Rajapakse, K. Lasek, I. Píš, F. Bondino and M. Batzill, *Appl. Surf. Sci.*, 2024, **644**, 158785, DOI: [10.1021/acsnano.2c04303](https://doi.org/10.1021/acsnano.2c04303).
- 18 S. Pan, M. Hong, L. Zhu, W. Quan, Z. Zhang, Y. Huan, P. Yang, F. Cui, F. Zhou, J. Hu, F. Zheng and Y. Zhang, *ACS Nano*, 2022, **16**, 11444–11454, DOI: [10.1021/acsnano.2c05570](https://doi.org/10.1021/acsnano.2c05570).
- 19 *Open Quantum Materials Database*, <https://oqmd.org/materials/entry/13823>, (accessed 05/04/2025).
- 20 J. J. Yeh and I. Lindau, *At. Data Nucl. Data Tables*, 1985, **32**, 1–155, DOI: [10.1016/0092-640X\(85\)90016-6](https://doi.org/10.1016/0092-640X(85)90016-6).
- 21 G. Drera, G. Salvinelli, J. Åhlund, P. G. Karlsson, B. Wannberg, E. Magnano, S. Nappini and L. Sangaletti, *J. Electron Spectrosc. Relat. Phenom.*, 2014, **195**, 109–116, DOI: [10.1016/j.elspec.2014.06.010](https://doi.org/10.1016/j.elspec.2014.06.010).
- 22 J. P. Perdew, K. Burke and M. Ernzerhof, *Phys. Rev. Lett.*, 1996, **77**, 3865–3868, DOI: [10.1103/PhysRevLett.77.3865](https://doi.org/10.1103/PhysRevLett.77.3865).
- 23 G. Kresse and J. Furthmüller, *Phys. Rev. B: Condens. Matter Mater. Phys.*, 1996, **54**, 11169–11186, DOI: [10.1103/PhysRevB.54.11169](https://doi.org/10.1103/PhysRevB.54.11169).
- 24 D. Joubert, *Phys. Rev. B: Condens. Matter Mater. Phys.*, 1999, **59**, 1758–1775, DOI: [10.1103/PhysRevB.59.1758](https://doi.org/10.1103/PhysRevB.59.1758).
- 25 S. Grimme, J. Antony, S. Ehrlich and H. Krieg, *J. Chem. Phys.*, 2010, **132**, 154104, DOI: [10.1063/1.3382344](https://doi.org/10.1063/1.3382344).

